Research Square

Preprints are preliminary reports that have not undergone peer review.
They should not be considered conclusive, used to inform clinical practice,
or referenced by the media as validated information.

RAIBO2: Highly efficient quadruped robot completing full marathon with a single battery charge

Jemin Hwangbo

jhwangbo@kaist.ac.kr

KAIST

Choongin Lee

KAIST RAILAB https://orcid.org/0009-0009-7625-9952

Donghoon Youm

KAIST RAILAB

Jeongsoo Park

KAIST RAILAB

Jeonghyun Lee

KAIST RAILAB

Suyoung Choi

KAIST RAILAB

Gwanghyeon Ji

KAIST RAILAB

Juhyeok Mun

KAIST RAILAB

Moonkyu Jung

KAIST RAILAB

Hyungho Chris Choi

KAIST RAILAB https://orcid.org/0000-0002-4758-2007

Hyeongjun Kim

KAIST RAILAB

Hyunsik Oh

KAIST RAILAB

Kyeongmin Nam

KAIST RAILAB

Minho Lee

KAIST RAILAB https://orcid.org/0009-0002-4930-1042

Jungwoo Hur

KAIST RAILAB https://orcid.org/0009-0004-3641-355X
Donghyuk Choi
KAIST RAILAB
Donggeon Kim
KAIST RAILAB https://orcid.org/0009-0000-8926-4579
Yeonsu An
KAIST RAILAB

Physical Sciences - Article

Keywords:

Posted Date: March 26th, 2025

DOI: https://doi.org/10.21203/rs.3.rs-6040970/v1

License: This work is licensed under a Creative Commons Attribution 4.0 International License.
Read Full License

Additional Declarations: There is **NO** Competing Interest.

RAIBO2: Highly efficient quadruped robot completing full marathon with a single battery charge

Choongin Lee[1*], Donghoon Youm[1*], Jeongsoo Park[1*], Jeonghyun Lee[1], Suyoung Choi[1], Gwanghyeon Ji[1], Juhyeok Mun[1], Moonkyu Jung[1], Hyungho Choi[1], Hyeongjun Kim[1], Hyunsik Oh[1], Kyeongmin Nam[1], Minho Lee[1], Jungwoo Hur[1], Donghyuk Choi[1], Donggeon Kim[1], Yeonsu An[1] and Jemin Hwangbo[1+]

[1] *Robotics and Artificial Intelligence Lab, KAIST, Daejeon, Korea*

[*] *Authors contributed equally to this work*

[+] *To whom correspondence should be addressed: jhwangbo@kaist.ac.kr*

Recent advances in legged robot control have expanded the potential for quadrupedal robots in real-world applications, such as rescue operations in disaster zones and mountainous regions. However, practical deployment is hindered by the limited travel range per battery charge—a challenge compounded by the robots' inherent structural characteristics. Unlike wheeled robots, quadrupeds continuously expend energy at their joints to support body weight and incur kinetic energy losses during intermittent foot–ground contact. Moreover, optimizing energy consumption is complicated by trade-offs among various physical effects, necessitating a holistic approach that optimizes both hardware and software components. Prior research has predominantly addressed isolated aspects of energy loss. In this work, we present RAIBO2, an energy-efficient quadruped designed through a comprehensive analysis of its energy loss model. Efficiency is enhanced via a force-transparent, lightweight mechanical hardware, a low-loss motor driving circuit, and an energy-optimized locomotion policy. RAIBO2 completed a full marathon in 4 hours, 19 minutes, and 52 seconds on a single battery charge, achieving a Total Cost of Transport (TCOT) of 0.25—the first quadrupedal robot to surpass the human benchmark of 0.37. Compared to existing quadrupeds, RAIBO2 of-

fers more than *three times* the travel range per battery charge. This breakthrough in energy efficiency paves the way for extended outdoor applications where prolonged battery life is critical.

Main text

Quadruped robots have recently made significant strides in mobility, particularly in high-speed locomotion[1–5] and terrain adaptation[6–8], which enhance their potential for deployment in real-world outdoor environments, such as rescue operations in mountainous or disaster-stricken areas. However, these outdoor missions often require robots to operate for extended periods and cover long distances. Current legged robots remain limited in their ability to operate beyond a range of 20 km[9]. To fully unlock the potential of legged robots, it is crucial to further extend their operational range on a single battery charge.

Improving locomotion efficiency in quadruped robots to extend their travel distance is more challenging than in wheeled robots. Quadruped robots must continuously expend energy at the joints to support their body weight and experience additional kinetic energy losses during intermittent foot-ground contact. These robots also face complex trade-offs between various loss components and the interconnected effects of multiple design parameters[10–13]. One significant challenge in optimizing energy loss in quadruped robots lies in the trade-off between actuator electrical loss and foot collision loss. Actuator electrical loss arises from the joint torques needed to support the robot's body mass, whereas foot collision loss occurs as kinetic energy dissipates during foot-ground impact when repositioning the feet. Design strategies to reduce actuator electrical loss, such as increasing gear ratios[14] or raising the body height[15], increase the apparent inertia of the foot, thereby leading to greater foot collision losses, and vice versa. As such, the design process must carefully consider the interrelationships between these elements while striving to minimize total energy loss.

Previous research on enhancing quadruped locomotion efficiency has yielded incremental improvements in specific aspects of legged robots, such as mechanical design optimization[13,14,16], locomotion posture optimization[15], and gait adaptation through reinforcement learning (RL)[17,18].

However, no study has adopted a comprehensive approach that integrates hardware design and locomotion policy on a single platform. A more holistic optimization strategy could achieve superior efficiency by incorporating multiple design parameters within a single platform. This approach requires a systematic analysis of losses and their relationships with design parameters in the mechanical, electrical, and control domains, allowing a complete optimization of the entire system.

In this paper, we propose an energy-efficient quadruped robot system, RAIBO2 (Fig. 1a). RAIBO2 improves efficiency by optimizing a wide range of design variables across mechanical hardware, electrical circuits, and locomotion behavior on a single platform. Through detailed loss modeling and analysis of relationships between losses and design variables, we identified key design factors that impact the efficiency of the quadruple robot in all domains (Fig. 1b). We incorporated established design strategies of force transparent actuators [12], lightweight legs [11], high motor constant motors [14], and efficient locomotion posture [15]. Our additional efficiency gains came from optimized motor driving circuits and a locomotion policy trained with reinforcement learning (RL).

We validated RAIBO2's performance by participating in a full marathon (Fig. 1c), completing the 42.195 km course in 4 hours, 19 minutes, and 52 seconds [19,20], with an energy consumption of 1280 Wh (Supplementary Video 4). Based on the data, the robot was capable of traveling 67 kilometers with a total battery capacity of 2016 Wh. RAIBO2 achieved a total cost of transport (TCOT) [21] — the energy consumed in Joules per meter and per kilogram-force — of 0.25 (Fig. 1d), becoming the first quadruped robot to surpass human TCOT (0.37). Furthermore, the robot demonstrated approximately *three times* the travel distance (km) per battery charge (Wh) compared to that of recent state-of-the-art quadruped robots (Fig. 1e).

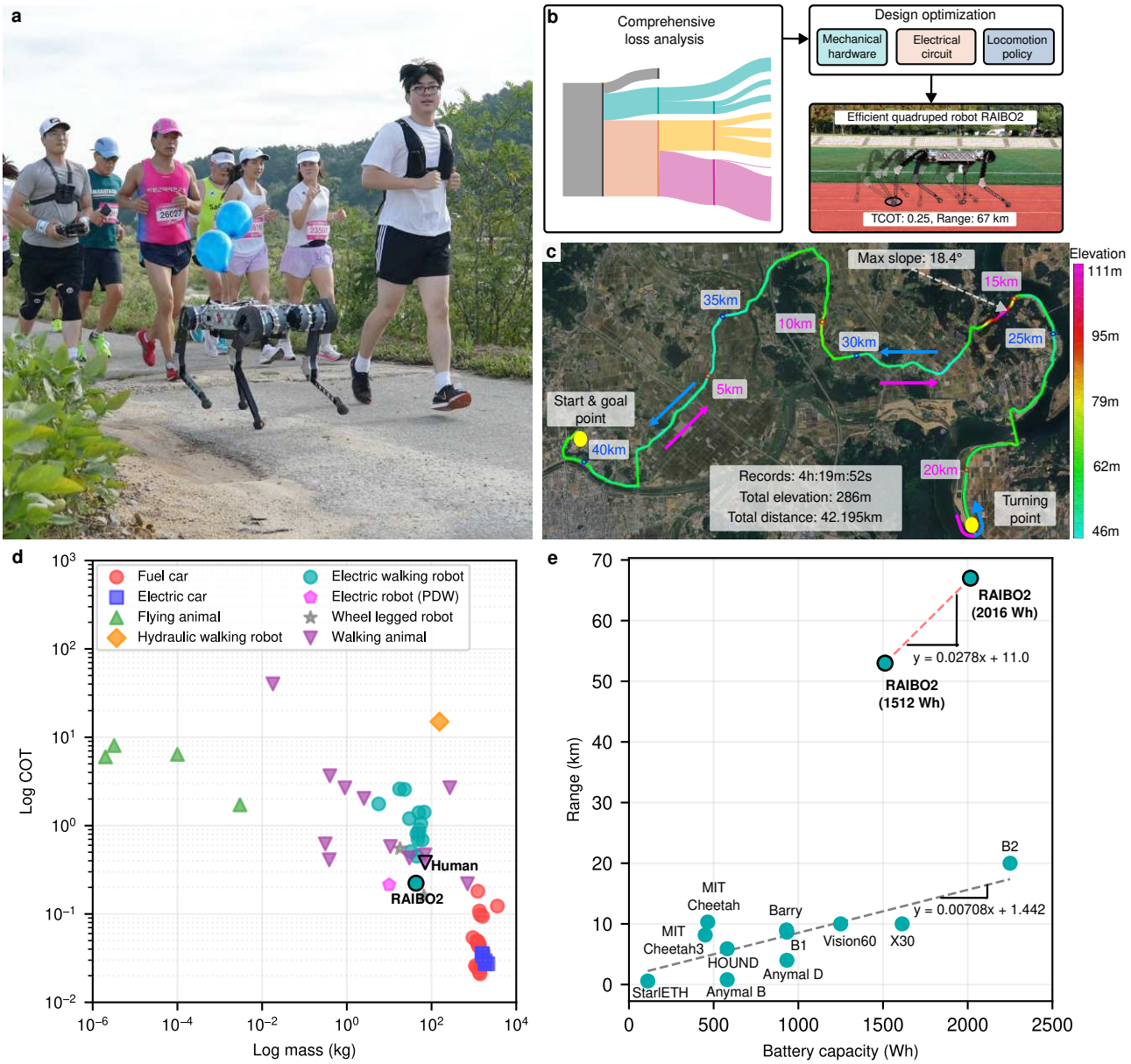

Fig.1 | Demonstration of RAIBO2's exceptional marathon performance and energy efficiency in real-world operation. **a,** RAIBO2 demonstrating outdoor locomotion capabilities alongside human runners (Supplementary Video 1). **b,** Design optimization framework showing comprehensive loss analysis leading to system-wide improvements across mechanical, electrical, and locomotion policy domains, achieving a Total Cost of Transport (TCOT) of 0.25 and a range of 67 km. **c,** Marathon course profile showing the successful completion of a full 42.195 km marathon without battery replacement. The challenging route features significant elevation changes totaling 286 m and a maximum slope of 18.4 degrees. **d,** Cost of Transport (COT) comparison across various locomotion systems plotted against mass, demonstrating RAIBO2's exceptional efficiency with COT lower than humans[9,12,14,16,21–38]. **e,** Range versus battery capacity plot showing RAIBO2's superior performance among quadrupedal robots, achieving over three times the distance per battery capacity compared to the regression trend of existing platforms[9,12,14,16,30,32,33,35–38].

System overview

RAIBO2, designed through comprehensive loss analysis, incorporates efficiency improvements across mechanical hardware, electrical circuits, and locomotion policy domains. Fig. 2 illustrates the key features implemented in each domain to enhance overall system efficiency in our proposed quadruped robot.

In mechanical hardware design, RAIBO2 consists of four identical legs with three identical actuators per leg, creating a modular system, as shown in Fig. 2a. Our key focus on improving efficiency is a high force transparent actuator and low leg inertia, based on a proprioceptive actuation philosophy[11,12,33]. To achieve this, we utilized a four-bar linkage mechanism at the knee joint transmission and a single-stage planetary gear (7.15:1) at the actuator reducer. With a lightweight leg mechanism (1.1 kg), the robot's design was optimized for minimal weight, with leg mechanisms accounting for 10.2 percent of the total robot weight (Extended Data Table. 1).

In terms of electrical design, RAIBO2 uses Brushless DC (BLDC) motors, which are driven by a motor driver Printed Circuit Board (PCB) consisting of an MCU, gate driver, and a 3-phase 2-level inverter with 6 MOSFETs (Fig. 2b). In motor driver circuit design, we aimed to minimize motor driver losses by reducing both conduction losses from circuit resistance and switching losses from MOSFET operation. To reduce resistive components in the motor driver circuit, we utilized 2 oz PCB copper thickness for all layers and designed with low turn-on resistance MOSFETs and low resistance Hall-effect current sensors. Additionally, gate resistors were minimized to reduce switching losses while preventing an oscillatory response.

The locomotion control policy is implemented in a hierarchical structure with the motor control algorithm as shown in Fig. 2c, controlling the legs through the BLDC motors. The locomotion policy network consists of a cascaded Gated Recurrent Unit (GRU) network and a Multi-Layer Perceptron (MLP) network[4], which utilizes proprioceptive sensor data as observations. The rewards

for RL-based network training focus on three categories: command tracking reward, locomotion style reward, and energy minimization reward. The energy minimization reward includes foot pre-contact velocity minimization for foot collision loss reduction and magnetic saturation-aware current minimization for motor copper loss reduction. Detailed network architecture and training methods are described in the methods section.

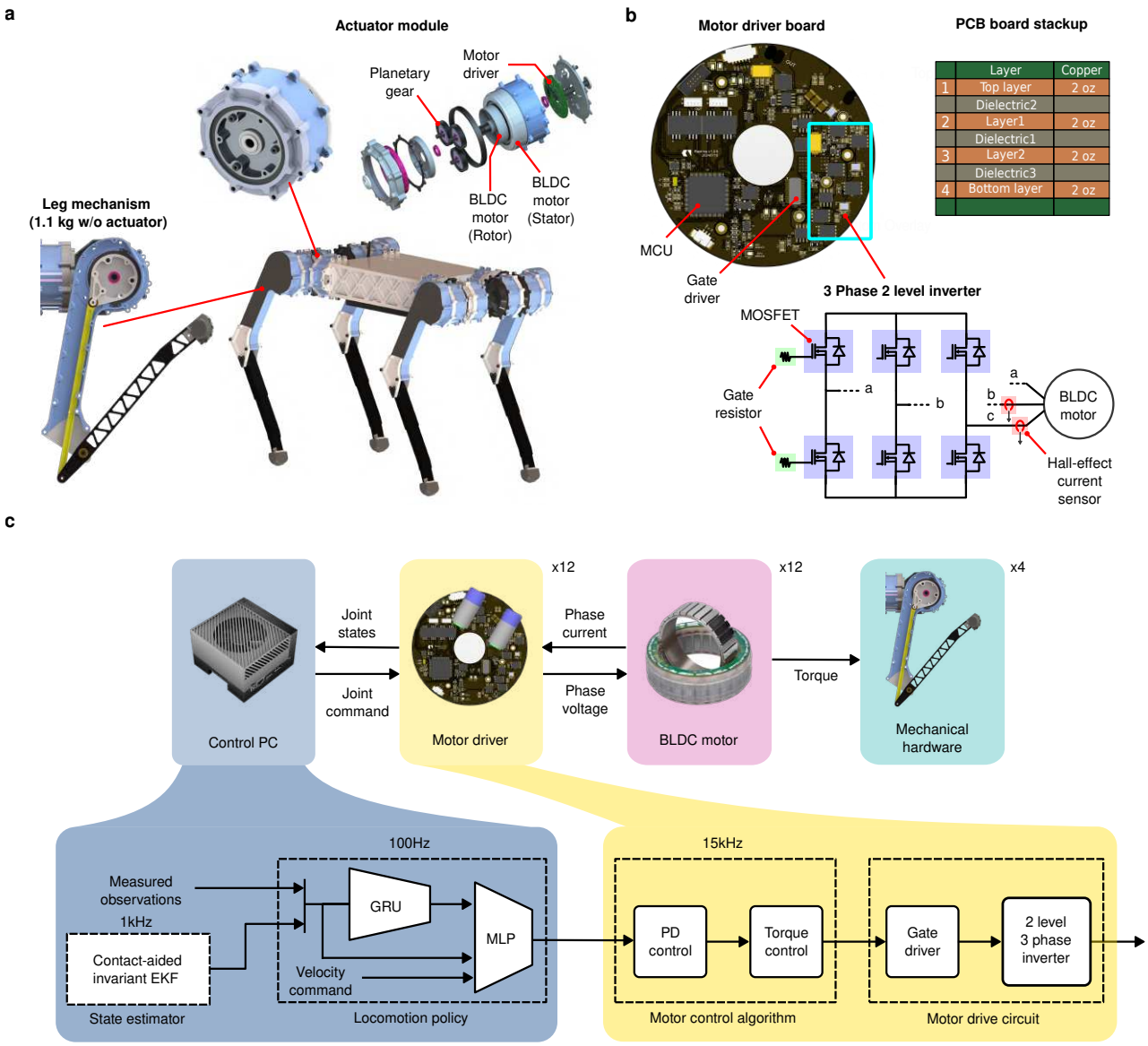

Fig.2 | System overview of RAIBO2. a, Energy efficiency mechanical hardware system featuring a lightweight leg mechanism (1.1 kg without actuator) and force transparent actuator module. The modular actuator design integrates a motor driver, brushless DC motor, and single-stage planetary gear transmission into a compact unit. **b,** Low-loss motor driver board design and circuit configuration. The PCB stackup utilizes 2 oz copper layers to minimize conduction losses, with a simplified schematic showing the 3-phase 2-level inverter motor driver circuit incorporating Hall-effect current sensing. **c,** System architecture showing the hardware integration and control hierarchy. The control PC coordinates twelve motor drivers and actuators through real-time communication (2 kHz). The hierarchical control structure implements a contact-aided invariant EKF for state estimation[39], GRU-based locomotion policy (100 Hz), and cascaded motor control algorithms (15 kHz), including PD control and torque control, culminating in gate driving of the 2-level 3-phase inverter.

Quadruped robot loss analysis

To improve the efficiency of quadruped robots, we first developed a comprehensive understanding of quadruped robot losses. In this section, we present a detailed breakdown of loss components in quadruped robot systems. Then, we analyze the relationships between these individual losses and key design factors across the mechanical, electrical, and locomotion domains to establish design principles for efficient quadruped robot systems.

We categorized the total losses in quadruped robots into three main components: system loss, mechanical loss, and actuator electric loss. The mechanical loss is further divided into slip loss, collision loss, and joint friction loss, while the actuator electric loss is subdivided into driver loss and motor loss. A more detailed breakdown of these losses is presented in the Sankey diagram in Fig. 3a, which shows the loss distribution when RAIBO2 achieves its lowest cost of transport (COT) during locomotion at 3m/s. The methods used to measure each loss component are described in the Methods section.

System loss accounts for 9.6 percent of total losses and represents the baseline power consumption required for robot system operation. It encompasses power consumption from multiple sources: PC operation loss for control algorithms, device operation loss such as IMU and communication Hub, and Joule loss from the power distribution board.

Mechanical loss, which accounts for 22.7 percent of total losses, can be categorized into friction-based and collision-based losses. Friction-based losses include joint friction loss and slip loss, with collision-based loss occurring through foot collision. This mechanical loss exhibits the steepest increase with velocity (Fig. 3b) and is the primary factor causing COT to rise after 3 m/s (Fig. 3c).

Slip loss, accounting for 2.9 percent of total losses, occurs from the sliding motion between foot and ground during the stance phase. Slipping initiates when the horizontal ground force

exceeds the maximum static friction force (product of static friction coefficient and normal force). This necessitates controlling stance phase force direction within specific angles. Over-extended legs reduce manipulability, making slip suppression difficult and resulting in increased locomotion losses or decreased stability. Our RL-based policy training methodology achieves stable 3 m/s locomotion up to 86 percent of full leg extension but fails to maintain higher postures (Fig. 3g).

Foot collision loss represents 8.4 percent of total losses, occurring as kinetic energy dissipation at impact (Fig. 3d). This loss is determined by both pre-contact velocity and apparent inertia of the foot. Pre-contact velocity can be controlled as part of locomotion behavior, but achieving zero foot velocity at impact remains challenging due to the need for precise foot contact timing prediction. The RL-based controller addresses this challenge by incorporating contact information into the critic network's observations, effectively reducing mechanical loss through negative rewards (Fig. 3f and Supplementary Video 2).

Joint friction loss, contributing 13.4 percent of total losses, occurs in the relative motion between gear teeth used for torque amplification and serves as a key indicator of actuator force transparency. Gear friction is modeled using the Coulomb friction model, where frictional force is proportional to the normal force at the gear contact points. Design factors influencing gear friction loss include the number of gear stages, pressure angle[40]. Implementing single-stage planetary gear transmissions and reducing normal force through lightweight leg design or elevated gait postures contribute to the reduction of joint friction losses.

Another notable aspect of the locomotion is that the stance phase exhibits an energy flow pattern similar to human walking, in which muscles store and release energy through active tension[41], with distinct generating and motoring phases (t1 to t2 and t2 to t3, respectively, in Fig. 3d). The controlled electrical stiffness mimics mechanical spring behavior[30,31,42,43]: energy absorption during compression creates near-inelastic collisions for stable contact, and the stored energy is subsequently utilized for robot propulsion. The energy flow pattern emerges not only within individual

leg gait cycles but also in the coordinated interaction between the front and rear legs. Analysis of the front right leg and rear left leg, which are synchronized in trot gait, reveals specialized roles in energy distribution: the front leg predominantly handles energy generation, and the rear leg focuses on propulsion (Fig. 3e).

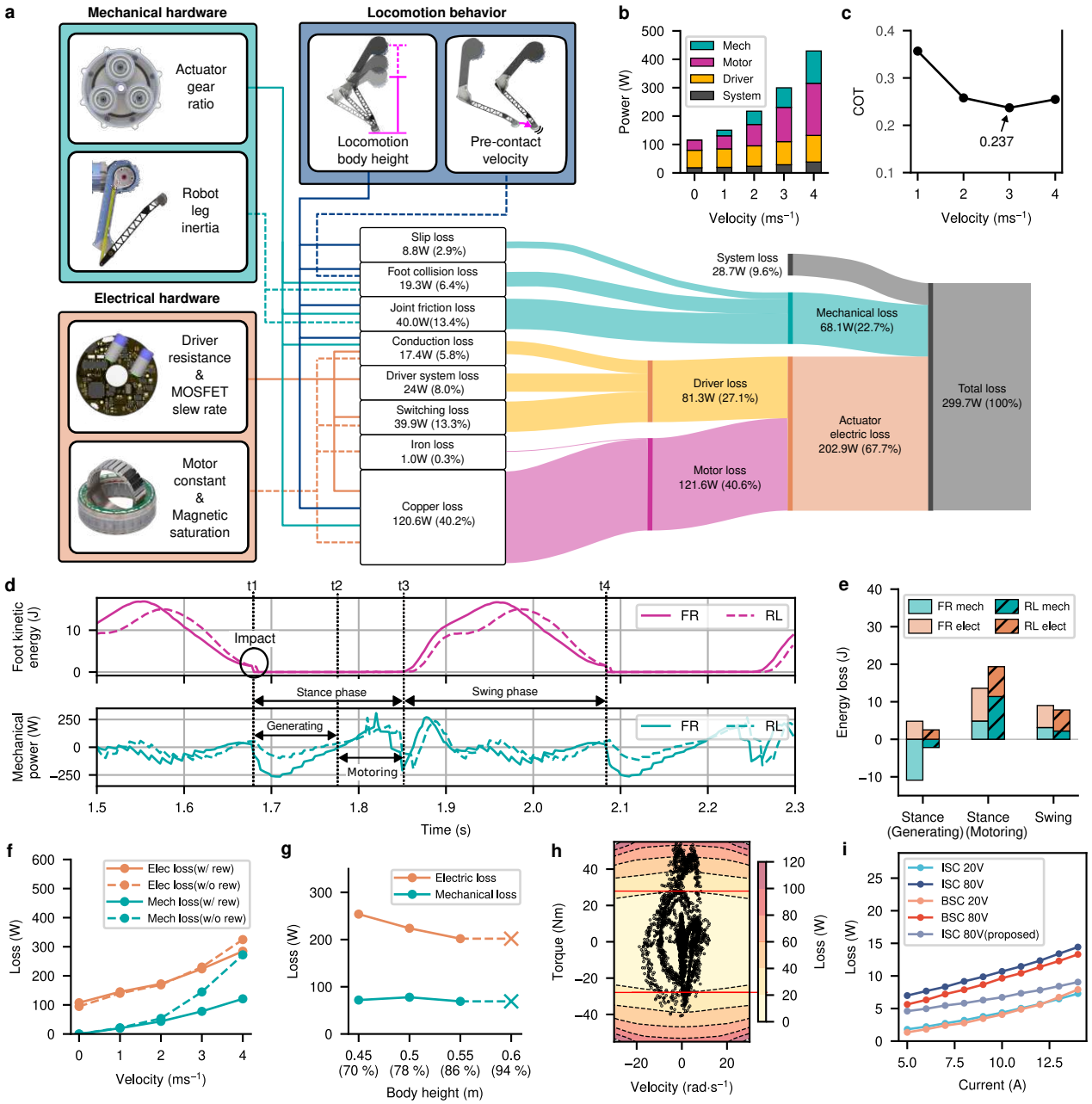

Fig.3 | Comprehensive loss analysis of RAIBO2 (with 1512 Wh). a, Sankey diagram depicting power loss distribution (299.7 W) during locomotion at 3 m/s, with connecting lines showing relationships between key design factors and loss components. **b,** Stacked bar chart showing velocity-dependent loss composition. **c,** Velocity-dependent Cost of Transport (COT), reaching a minimum of 0.237 at 3 m/s. **d,** Single gait cycle analysis showing foot kinetic energy and mechanical power for Front Right (solid) and Rear Left (dashed) legs. **e,** Energy loss distribution across gait phases for Front Right and Rear Left legs. **f,** Impact of foot collision loss reward on mechanical and electrical losses across velocities. **g,** Effect of body height on mechanical and electrical losses, demonstrating trade-off relationship (numbers in parentheses indicate percentage relative to full leg extension). **h,** Motor operating points during optimal locomotion overlaid on power loss colormap, with dashed lines indicating equal loss contours and a red solid line showing rated torque boundary. **i,** Comparative analysis of driver losses for two MOSFET types (BSC and ISC) at high (80V) and low (20V) voltage conditions across varying currents.

The actuator electric loss, representing 67.7 percent of total losses, occurs as heat dissipation in the motor and motor driver circuitry. Motor losses comprise copper loss and iron loss; motor driver losses include system loss, conduction loss, and switching loss. As this actuator electric loss is primarily determined by motor current, it is influenced by all design elements affecting required motor current across locomotion behavior, mechanical hardware, and electrical hardware.

From a locomotion behavior perspective, quadruped robots generate foot end-effector forces to support and propel their bodies. Higher body positions enable the same end-effector forces with reduced joint torques, resulting in lower actuator electric losses (Fig. 3g and Supplementary Video 3). In mechanical hardware design, gears serve as torque amplifiers between motor torque and joint torque. Increased gear ratio reduces required motor torque for equivalent joint torque output, decreasing actuator electric loss. From the electrical hardware perspective, motor structure and motor driver component selection are key design parameters.

Motor copper loss, accounting for 40.2 percent of total losses, occurs in stator resistance during magnetic field generation for torque production. Efficient torque generation demands high torque density per current and low phase resistance. These two characteristics define the motor constant ($\mathrm{Nm}/\sqrt{\mathrm{W}}$), a key parameter for motor selection in reducing copper loss for quadruped robot design[14]. However, increasing torque density through additional winding turns and reducing phase resistance through thicker conductors both require more copper content. The extra copper mass increases robot weight and torque requirements, making it essential to select motors with high motor constant within given weight constraints.

Copper loss is also affected by motor magnetic saturation. Motors use iron stator slots to amplify torque through ferromagnetic dipole alignment. Rated torque marks the beginning of magnetic saturation, where magnetic dipoles become saturated and produce diminishing torque gains per current increment, reducing motor constant. Larger iron slots delay this saturation point but increase robot weight, necessitating careful motor selection. In our study, during lowest TCOT

locomotion at 3m/s, 84.1 percent of operation remains within rated torque limits (Fig. 3h).

Motor iron loss, accounting for 0.3 percent of total losses, occurs in rotor and stator iron used for magnetic field alignment and amplification. This loss increases with magnetic field magnitude and frequency, with its coefficients determined by motor geometry and material properties[44]. In our study, the selected motor demonstrated minimal iron losses in its operating range. Additionally, our trained controller rarely required simultaneous high-speed and high-torque operation, contributing to low iron losses.

Driver conduction loss, accounting for 5.8 percent of total losses, arises from ohmic losses in current-carrying conductors and components of the motor driver PCB. The current path components in the motor driver circuit include PCB copper, MOSFETs, and current sensors, where reducing their resistance contributes to decreasing the current-squared term of driver losses. The loss reduction effects from decreased resistance in each component are demonstrated in Extended Data Fig. 2c, d, and f.

Driver switching loss represents 13.3 percent of total losses occurring during MOSFET state transitions for PWM control. This loss depends linearly on load current and is affected by battery voltage, MOSFET state transition time, and switching frequency[45,46]. As shown in Fig. 3i, the comparison between ISC 20V and ISC 80V waveforms demonstrates the impact of battery voltage on losses. The ISC 80V (proposed) waveform shows reduced switching losses through lower switching frequency and shorter transition times, which is evident when compared to the ISC 80V waveform. Detailed parameter settings are provided in the Methods section.

Efficiency validation through full marathon completion

RAIBO2 completed the full marathon of the 22nd Sangju Gotgam Marathon to demonstrate its operating range experimentally (Supplementary Video 4). The Sangju marathon course, with its 286 m total elevation and slopes approaching 18 degrees (Fig. 4i and j), is known as one of the most challenging marathon courses in Korea. The marathon course, shown in Fig. 4b, was a round-trip route with a turning point in the middle. As evident from Fig. 4a-d, most of the course consisted of asphalt roads, including slippery sections covered in fallen leaves.

The detailed data collected during the marathon are presented in Fig. 4e-h. The robot completed the whole 42.195 km distance in 4 hours, 19 minutes, and 52 seconds at an average speed of 2.64 m/s [19,20]. The power and battery data (Fig. 4g and h) show that the robot consumed 1280 Wh of energy throughout the marathon, corresponding to an average TCOT of 0.248, which aligns with previously demonstrated efficiency metrics (Fig. 3c). This energy consumption represents 63 percent of the total 2016 Wh battery capacity (Fig. 4e). The data indirectly validate the robot's theoretical ability to traverse up to 67 km.

Despite the 286 m total elevation gain, one factor enabling high efficiency is RAIBO2's ability to regenerate mechanical energy during descents. Loss analysis during 3 m/s locomotion on level ground, a 7-degree incline, and a 7-degree decline (Fig. 4k) demonstrates an additional mechanical loss of 100.5 W on inclines while recovering 107.5 W on declines. The increased energy consumption during uphill is compensated by energy regeneration during the downhill locomotion, as evidenced by the generating phases in the power profiles (Fig. 4l).

The comprehensive dataset from the full-course marathon trial provides valuable insights into RAIBO2's robust and energy-efficient performance in real-world outdoor conditions, validating its capabilities for practical deployment.

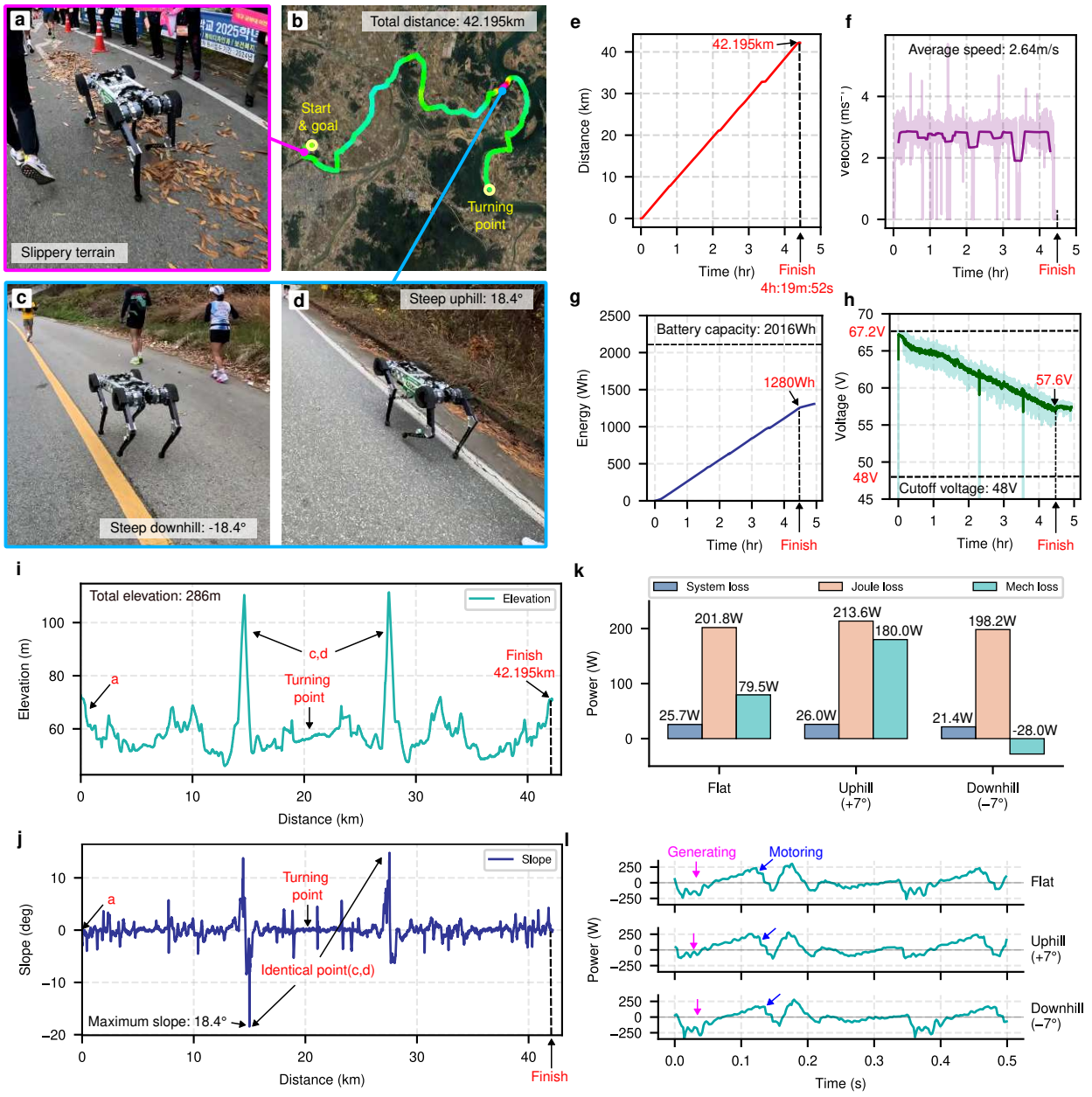

Fig.4 | **Marathon completion data analysis.** **a,** RAIBO2 navigating challenging slippery terrain covered with fallen leaves. **b,** Satellite view of the 42.195 km marathon course showing the start/goal point and turning point. **c,d,** Robot traversing steep gradients of -18.4° (downhill) and +18.4° (uphill) respectively. **e,f,** GPS tracking data showing distance covered over time and velocity profile with an average speed of 2.64 m/s. **g,h,** Energy consumption metrics from the power board: total energy usage of 1280 Wh from 2016 Wh battery capacity, and battery voltage drop from 67.2 V to 57.6 V. **i,j,** Elevation and slope profiles along the course, highlighting total elevation change of 286 m and maximum slopes of ±18.4°. **k,** Power loss composition analysis across different terrain conditions (flat, uphill +7°, downhill -7°). **l,** Mechanical power waveforms showing generating and motoring phases during locomotion on varying slopes. The robot efficiently regenerates energy during downhill sections while maintaining stable control across all terrain conditions.

Discussion

Our work demonstrates that holistic design optimization through comprehensive energy analysis can achieve energy efficiency far beyond what has been presented in the existing literature. Previous studies have focused on incremental improvements in isolated aspects of legged robots, mainly due to the partial understanding of the loss composition in quadruped robots. Based on our measurement-driven analysis of comprehensive loss structures, we improved efficiency across the mechanical, electrical, and control domains, identifying critical elements for enhancing locomotion efficiency in each design aspect.

In mechanical design, we focused on two key aspects: force transparency and lightweight leg design. Force transparency affects both joint friction loss and energy conversion efficiency during the regenerating-motoring cycles of gait. Leg inertia impacts both joint friction loss and foot collision losses. In the electrical domain, motor selection and driver circuit design proved crucial. We selected motors with high motor constants and operations below magnetic saturation limits. Also, we designed the motor driver with low-resistance component selection for low conduction loss and increased MOSFET state transition slew rate to reduce switching loss. For locomotion behavior, we concentrated on reducing both foot collision and actuator electric loss. Through reinforcement learning reward formulation, we achieved a lower pre-contact velocity and minimized current usage in magnetic saturation regions.

Several challenges remain to be addressed. Our study employs blind controllers optimized for minimal losses in typical locomotion scenarios, but specialized environments like stairs or mountainous terrain present varying loss models and constrained robot postures, necessitating the development of environment-aware efficient locomotion strategies. Additionally, our study assumes human operation, yet autonomous navigation requires planners that can identify energy-optimal paths based on global map understanding. The loss models developed in this study provide

a valuable foundation for addressing these challenges.

The insights and methodologies developed in this study extend beyond quadrupedal systems, offering valuable principles for reducing losses in various motor-driven robotic applications. We anticipate that these findings will contribute to expanded operational ranges and broader deployment of mobile robots, particularly in emerging platforms such as bipedal and wheel-legged systems, where efficiency directly impacts practical utility.

Main references

[1] Park, H.-W., Wensing, P. M. & Kim, S. High-speed bounding with the mit cheetah 2: Control design and experiments. The International Journal of Robotics Research **36**, 167–192 (2017).

[2] Agility Robotics. Cassie bipedal robot. Agility Robotics, Corvallis, Oregon (2017). All-electric bipedal robot designed for research and development in locomotion.

[3] Jin, Y., Liu, X., Shao, Y., Wang, H. & Yang, W. High-speed quadrupedal locomotion by imitation-relaxation reinforcement learning. Nature Machine Intelligence **4**, 1–11 (2022).

[4] Ji, G., Mun, J., Kim, H. & Hwangbo, J. Concurrent training of a control policy and a state estimator for dynamic and robust legged locomotion. IEEE Robotics and Automation Letters **7**, 4630–4637 (2022).

[5] Shin, Y.-H., Song, T.-G., Ji, G. & Park, H.-W. Reinforcement learning for high-speed quadrupedal locomotion with motor operating region constraints: Mitigating motor model discrepancies through torque clipping in realistic motor operating region. IEEE Robotics & Automation Magazine 2–13 (2024).

[6] Lee, J., Hwangbo, J., Wellhausen, L., Koltun, V. & Hutter, M. Learning quadrupedal locomotion over challenging terrain. Science robotics **5**, eabc5986 (2020).

[7] Choi, S. et al. Learning quadrupedal locomotion on deformable terrain. Science Robotics **8**, eade2256 (2023).

[8] Miki, T. et al. Learning robust perceptive locomotion for quadrupedal robots in the wild. Science Robotics **7**, eabk2822 (2022).

[9] Unitree Robotics. Unitree b2: Go beyond the limits. Online: `https://www.unitree.com/b2` (2023).

[10] McGeer, T. Dynamic walking robots and the w prize [industry/research news]. IEEE Robotics and Automation Magazine **14**, 13–15 (2007).

[11] Wensing, P. M. et al. Proprioceptive actuator design in the mit cheetah: Impact mitigation and high-bandwidth physical interaction for dynamic legged robots. IEEE Transactions on Robotics **33**, 509–522 (2017).

[12] Seok, S. et al. Design principles for energy-efficient legged locomotion and implementation on the mit cheetah robot. IEEE/ASME Transactions on Mechatronics **20**, 1117–1129 (2015).

[13] Kitano, S., Hirose, S., Horigome, A. & Endo, G. Titan-xiii: sprawling-type quadruped robot with ability of fast and energy-efficient walking. Robomech Journal **3**, 1–16 (2016).

[14] Valsecchi, G. et al. Barry: A high-payload and agile quadruped robot. IEEE Robotics and Automation Letters **8**, 6939–6946 (2023).

[15] Chen, L. et al. Optimized foothold planning and posture searching for energy-efficient quadruped locomotion over challenging terrains. In 2020 IEEE International Conference on Robotics and Automation (ICRA), 399–405 (2020).

[16] Shin, Y.-H. et al. Design of kaist hound, a quadruped robot platform for fast and efficient locomotion with mixed-integer nonlinear optimization of a gear train. In 2022 International Conference on Robotics and Automation (ICRA), 6614–6620 (2022).

[17] Fu, Z., Kumar, A., Malik, J. & Pathak, D. Minimizing energy consumption leads to the emergence of gaits in legged robots. arXiv preprint arXiv:2111.01674 (2021).

[18] Yang, Y., Zhang, T., Coumans, E., Tan, J. & Boots, B. Fast and efficient locomotion via learned gait transitions. In Conference on robot learning, 773–783 (PMLR, 2022).

[19] SPCT Co., Ltd. 22nd sangju gotgam marathon record system. Online: `https://time.spct.kr/m2.php?EVENT_NO=20241117017&TargetYear=2024&`

currentPage=1&BIB_NO=042004 (2024). Full course (42.195km) record system for the 22nd Sangju Gotgam Marathon.

[20] RaiLab KAIST. (1x speed) raibo2 completes full marathon (42.195km) in 4:19:52 - world's first robot marathon record. Online: https://youtu.be/-HMFoa3g9nA (2024). Accessed: November 19, 2024.

[21] Tucker, V. A. The energetic cost of moving about: Walking and running are extremely inefficient forms of locomotion. much greater efficiency is achieved by birds, fish—and bicyclists. American Scientist **63**, 413–419 (1975).

[22] Bobbert, A. C. Energy expenditure in level and grade walking. Journal of Applied Physiology **15**, 1015–1021 (1960).

[23] Tucker, V. A. Energetic cost of locomotion in animals. Comparative Biochemistry and Physiology **34**, 841–846 (1970).

[24] EV Database. Ev database - compare electric vehicles. Online: https://ev-database.org/ (2025).

[25] Fuelly. Fuelly: Track and compare your mpg. Online: https://www.fuelly.com/car (n.d.).

[26] McGeer, T. Passive dynamic walking. The International Journal of Robotics Research **9**, 62–82 (1990).

[27] Bhounsule, P. et al. Low-bandwidth reflex-based control for lower power walking: 65 km on a single battery charge. The International Journal of Robotics Research **33**, 1305–1321 (2014).

[28] Li, Q., Liu, G., Tang, J. & Zhang, J. A simple 2d straight-leg passive dynamic walking model without foot-scuffing problem. In

2016 IEEE/RSJ International Conference on Intelligent Robots and Systems (IROS), 5155–5161 (2016).

[29] Lee, J. et al. Learning robust autonomous navigation and locomotion for wheeled-legged robots. Science Robotics **9**, eadi9641 (2024).

[30] Hutter, M. et al. Starleth: A compliant quadrupedal robot for fast, efficient, and versatile locomotion. In Adaptive mobile robotics, 483–490 (World Scientific, 2012).

[31] Ding, L., Wang, R., Feng, H. et al. Brief analysis of a Big-Dog quadruped robot. China Mechanical Engineering **23**, 505–514 (2012).

[32] Hutter, M. et al. Anymal - toward legged robots for harsh environments. Advanced Robotics **31**, 918–931 (2017).

[33] Bledt, G. et al. Mit cheetah 3: Design and control of a robust, dynamic quadruped robot. In 2018 IEEE/RSJ International Conference on Intelligent Robots and Systems (IROS), 2245–2252 (2018).

[34] Boston Dynamics. Spot - the agile mobile robot. Online: `https://bostondynamics.com/products/spot/` (2019).

[35] Unitree Robotics. Unitree b1: Land overlord. Online: `https://www.unitree.com/b1` (2022).

[36] ANYbotics. Meet anymal your new inspector (2021). URL `https://www.anybotics.com/robotics/anymal/`.

[37] Ghost Robotics. Vision 60: Agile and autonomous quadruped. Online: `https://www.ghostrobotics.io/vision-60` (2021).

[38] DEEP Robotics. X30: Industrial application quadruped robot. Online: https://deeprobotics.cn/en/index/product3.html (2023).

[39] Hartley, R., Jadidi, M. G., Grizzle, J. W. & Eustice, R. M. Contact-aided invariant extended kalman filtering for legged robot state estimation. arXiv preprint arXiv:1805.10410 (2018).

[40] Chang, L., Jeng, Y.-R. & Huang, P.-Y. Modeling and analysis of the meshing losses of involute spur gears in high-speed and high-load conditions. Journal of Tribology **135**, 011504 (2013).

[41] Margaria, R. Positive and negative work performances and their efficiencies in human locomotion. Internationale Zeitschrift f"ur angewandte Physiologie einschließlich Arbeitsphysiologie **25**, 339–351 (1968).

[42] Li, M., Jiang, Z., Guo, W. et al. Leg prototype of a bio-inspired quadruped robot. Robot **36**, 21–28 (2014).

[43] Shi, Y., Zhang, M. & Zhang, X. Design and analysis of quadruped robot's leg with flexible joints. Huazhong University of Science and Technology (Natural Science Edition) **45**, 17–22 (2017).

[44] Mi, C., Slemon, G. & Bonert, R. Modeling of iron losses of permanent-magnet synchronous motors. IEEE Transactions on Industry Applications **39**, 734–742 (2003).

[45] Lakkas, G. Mosfet power losses and how they affect power-supply efficiency. Analog Applications Journal SLYT664, Texas Instruments (2016). AAJ 1Q 2016.

[46] Gopalan, A. Calculating power dissipation for a h-bridge or half bridge driver. Tech. Rep. SLVA504A, Texas Instruments (2021). Originally published in February 2012, revised in July 2021.

Methods

Mechanical hardware design

Required joint torque and speed derivation We analyzed dynamic loading conditions during trotting to determine actuator torque requirements. In our modular design using identical actuators for all joints, we based our torque specifications on the knee actuator as it experiences the highest torque demands due to its structural role in supporting body weight and body vertical velocity deceleration. The knee actuator must sustain constant body weight support during continuous trotting locomotion, leading to our rated torque specification of

$$\tau_{\text{rated}} = \frac{mgL_{\text{calf}} \cos\left(\theta_{\text{knee}}/2\right)}{n_{\text{leg,trot}}} = 44.34 \text{ Nm} \tag{1}$$

where $m = 40$ kg is the robot mass, $g = 9.81$ m/s² is gravitational acceleration, $L_{\text{calf}} = 0.32$ m is the calf length, $\theta_{knee} = 90°$ and $n_{\text{leg,trot}} = 2$ is the number of supporting legs during trot gait. Peak torque requirements were determined from the most demanding phase of trot gait locomotion. During the initial stage of the stance phase, the knee joint generates impulse torque through controlled stiffness to decelerate the body's vertical velocity. We calculated this required impulse torque by considering the change in body momentum and the resulting impact force. With an assumed body deceleration (a_{body}) of $2g$, we derived the required peak torque as

$$\tau_{\text{peak}} = \frac{ma_{\text{body}}L_{\text{calf}} \cos\left(\theta_{\text{knee}}/2\right)}{n_{\text{leg,trot}}} = 88.68 \text{ Nm}. \tag{2}$$

Speed requirements were derived from the target locomotion velocity of 4 m/s. Following Raibert's heuristic[56] for foot placement, the foot position (x_f) combines a nominal term ($\frac{\dot{x}T_s}{2}$) for steady-state locomotion and a correction term ($k_{\dot{x}}(\dot{x} - \dot{x}d)$) for disturbance rejection through

$$x_f = \frac{\dot{x}T_s}{2} + k\dot{x}(\dot{x} - \dot{x}_d) \tag{3}$$

where $\dot{x}$ is the forward speed, T_s is the stance duration, $\dot{x}d$ is the desired forward speed, and $k\dot{x}$ is a feedback gain. Similarly, we expressed the maximum foot velocity relative to the body as the sum of nominal velocity and disturbance rejection velocity. Assuming equal stance and swing times and that the foot must travel twice the capture point length relative to the body during swing phase, we derived nominal velocity as $v_{\text{nominal}} = (v_{\text{body}} T_{\text{stance}}/2) \cdot 2/T_{\text{swing}} = v_{\text{body}}$. Setting the disturbance rejection velocity to v_{body}, we obtained the total required velocity as

$$v_{\text{foot}} = v_{\text{nominal}} + v_{\text{rejection}} = v_{\text{body}} + v_{\text{body}} = 8 \text{ m/s} \tag{4}$$

From this foot velocity, we determined the required joint angular velocity for the pitch axis, which experiences the highest velocity demands. With $L_{\text{e}} = \sqrt{2} L_{\text{calf}}$ in the nominal posture as shown in Extended Data Fig. 1a, we obtained

$$\omega_{\text{req}} = \frac{v_{\text{foot}}}{L_{\text{e}}} = 17.7 \text{ rad/s}. \tag{5}$$

Based on these calculations, we established actuator specifications with a rated continuous torque of 25 Nm, peak torque of 90 Nm, and maximum angular velocity of 20 rad/s (191 rpm). These initial design targets were subsequently validated through detailed analysis and testing during the development process.

Motor selection Aiming for a force-transparent proprioceptive actuator design[12], we targeted a single-stage reduction ratio below 10:1, necessitating a motor with approximately 2.5 Nm rated torque, 9 Nm peak torque and 1910 rpm maximum speed. Among motors meeting our rated torque, peak torque, and maximum speed requirements, we prioritized those with high motor constant k_{M} (Nm/$\sqrt{\text{W}}$), which can be defined as

$$k_{\text{M}} = \frac{k_{\text{T}}}{\sqrt{R}}, \tag{6}$$

where k_T represents the torque constant (Nm/A) and R is the phase resistance (Ω). The selected TQ group ILM115x25 motor, with a motor constant of 0.87 Nm/$\sqrt{\text{W}}$, offers rated torque of 3.9 Nm, peak torque of 12.7 Nm, and rated speed of 1400 rpm at 48 V (Extended Data Table. 1b). Given surplus torque capacity but limited speed, this necessitated selection of a transmission mechanism with gear ratio below 10:1.

Planetary gear mechanism design The gear ratio was selected based on joint requirements and motor specifications. The ILM115x25 motor has $\tau_{\text{m}} = 3.9$ Nm rated torque, $\tau_{\text{m,max}} = 12.7$ Nm peak torque, and $\omega_{\text{m}} = 1400$ rpm rated speed, with joint requirements of $\tau_{\text{j}} = 25$ Nm rated torque and $\tau_{\text{j,max}} = 90$ Nm peak torque. The minimum gear ratios determined from these specifications are $\eta = \tau_{\text{j}}/\tau_{\text{m}} = 6.41 : 1$ for rated torque and $\eta_{\text{max}} = \tau_{\text{j,max}}/\tau_{\text{m,max}} = 7.09 : 1$ for peak torque. The maximum gear ratio to satisfy the speed constraint is ($\omega_{\text{m}}/\omega_{\text{j}} = 7.34$). Based on these calculations, a gear ratio ($\eta = 7 : 1$) was selected to satisfy both torque and speed requirements.

The planetary gear design process balanced multiple constraints, primarily focusing on maintaining compact size while achieving the required reduction ratio. The ring gear's outer diameter was constrained to match the motor diameter (115 mm) to minimize actuator size and leg inertia. The gear module was set to 0.7 to accommodate increased peak torque requirements. The sun gear tooth count was kept above 17 to prevent undercutting and maintain adequate hollow shaft diameter. The tooth configuration must satisfy

$$N_{\text{ring}} - N_{\text{sun}} = 2N_{\text{planet}}, \tag{7}$$

$$\frac{N_{\text{ring}} + N_{\text{sun}}}{n_{\text{p}}} \in \mathbb{Z}, \tag{8}$$

where N_{ring}, N_{sun}, and N_{planet} represent the tooth counts of the ring, sun, and planetary gears respectively, and n_{p} is the number of planetary gears in the system. These constraints, combined with considerations for the Lewis factor and manufacturing feasibility, led to the final configuration

of 160-67-26 teeth (ring-planet-sun) with three planetary gears, yielding a 7.15:1 reduction ratio. The gear thickness can be determined using the simplified AGMA formula

$$\sigma = \frac{W_{\mathrm{t}}}{b m_{\mathrm{t}} Y} K_{\mathrm{v}}, \tag{9}$$

where W_t is the tangential load, b is the face width, m_{t} is the module, Y is the Lewis form factor, and K_v is the dynamic factor. This calculation resulted in a 10 mm thickness specification.

Light inertia leg design The inertia of the moving components of the leg is divided into the inertia of the rotor and that of other parts. Among these, the rotor's inertia significantly affects energy consumption, as it is proportional to the square of the gear ratio. Therefore, reducing the rotor's inertia is crucial. As shown in the actuator detail view of the Extended Data Fig. 1a, a hollow shaft structure was implemented in the sun gear, while a lightweight aluminum structure was used for the rotor hub to minimize inertia.

In addition, the design focused on reducing inertia in other components. A cross-roller bearing was utilized to ensure structural stability even when the link is supported at a single end rather than both ends, as depicted in the leg mechanism top view of the Extended Data Fig. 1a. Furthermore, needle roller bearings were used instead of ball bearings to reduce both the weight of the bearings and the size of the components that hold them. Individual component weights were further optimized through static analysis based on required torque (Extended Data Fig. 1a, side view).

Low loss motor driver circuit design

The motor driver circuit manages power transfer from battery to motor, comprising joint communication and power control sections (Extended Data Fig. 1b). Most losses occur during power control, making component selection and circuit layout in the power control section crucial.

Motor driver losses can be divided into two main categories: conduction loss and switching loss. Conduction loss is the Ohmic loss that occurs when current flows to generate magnetic fields for desired motor torque. Switching loss occurs during MOSFET state transitions required for real-time motor current control through rapid changes in motor phase voltage. Through experimental setups shown in Extended Data Fig. 2a and b, we measured motor driver losses under various conditions and reduced both conduction and switching losses.

Conduction loss reduction Motor driver conduction loss, following quadratic current dependency, occurs in the main current paths comprising current sensors, MOSFETs and PCB copper traces. These components enable motor current control through a closed loop: current sensors measure phase currents, the driver adjusts MOSFET state to control phase voltages, and current flows through PCB copper traces.

Current measurement in motor drivers commonly uses two approaches (locations shown in Extended Data Fig. 1b) shunt resistors with operational amplifier and hall-effect sensors. Shunt resistors offer direct loss reduction through decreased resistance values (Extended Data Fig. 2c). However, low resistance requires high amplification ratios, which amplify ground noise and degrade control quality. In contrast, hall-effect sensors provide advantages through electrical isolation between current path and sensor power supply. This isolation allows direct installation on phase lines with low ground noise sensitivity. Moreover, being non-resistive measurement devices, they can achieve stable high amplification ratios with conduction loss. The selected hall-effect sensor (ACS725LLCTR-50AB-T), with a conduction resistance of 1.5 mΩ, demonstrated losses comparable to a 1 mΩ shunt resistor configuration (Extended Data Fig. 2c).

The next method to reduce conduction loss is increasing PCB copper thickness. We compared driver conduction losses between commonly used 1 oz and 2 oz copper thicknesses (1 oz equals 0.035 mm copper thickness) while maintaining a total PCB thickness of 1.6 mm. The re-

sults, presented in Extended Data Fig. 2f, show an equivalent resistance reduction of approximately 1.8 mΩ. We selected 2 oz copper for the final design after confirming sufficient dielectric layer thickness for safe operation at maximum voltage of 100V. Detailed experimental conditions can be found in Extended Data Table. 4a.

Lastly, our approach to reduce conduction loss focuses on low-resistance MOSFET selection. MOSFET conduction loss is determined by turn-on resistance ($R_{\mathrm{DS,on}}$), which typically increases as package size decreases. We compared two Infineon MOSFETs with identical footprint and voltage ratings: BSC070N10NS5SC (BSC $R_{\mathrm{DS,on}}$=7 mΩ, Q_{g}=30 nC) and ISC022N10NM6 (ISC $R_{\mathrm{DS,on}}$=2 mΩ, Q_{g}=73 nC). The driver with BSC MOSFET showed an equivalent resistance approximately 33 mΩ higher than the driver with ISC MOSFET in terms of total conduction loss (Extended Data Fig. 2d).

Switching loss reduction Motor drivers primarily control current using six MOSFETs, making switching losses a significant component of total losses. Therefore, MOSFET selection based solely on resistance characteristics without considering switching losses can lead to increased total losses. MOSFET switching loss can be modeled as $P_{\mathrm{sw}} = V_{\mathrm{in}} I_{\mathrm{out}} f_{\mathrm{sw}} \frac{Q_{\mathrm{gs}}+Q_{\mathrm{gd}}}{I_{\mathrm{g}}}$ where V_{in} is the drain-to-source voltage, I_{out} is the drain current, f_{sw} is the switching frequency, Q_{gs} and Q_{gd} represent gate charges, and I_{g} is the gate current[45,46]. At 80V operation, the driver with ISC MOSFET with larger gate charge exhibits higher total losses across all current ranges compared to the driver with BSC MOSFET despite its lower resistance (Extended Data Fig. 2e).

Our first approach to reduce switching losses focused on increasing gate current (I_{g}) by reducing gate resistance, which serves as a damping element for oscillatory gate signals. This resistance value, typically a tuning parameter determined by circuit resonance, can be minimized through circuit layout optimization that reduces parasitic inductance. The gate driver (Infineon 6EDL04N02PR) evaluation board datasheet specifies 180 Ω[51], but our improved circuit design al-

lowed reduction to 10 Ω. The resulting power reduction is demonstrated in Extended Data Fig. 2g.

Our second approach involved reducing switching frequency, which determines how often MOSFET states change and affects control performance. Under the 2 kHz master-slave communication, we lowered the switching frequency from 20 kHz to 15 kHz. Lower switching frequencies improve efficiency, as shown in Extended Data Fig. 2h, but we maintained 15 kHz to balance power efficiency with control performance requirements.

Locomotion policy training

Our locomotion policy training framework is illustrated in Extended Data Fig. 3a. We trained the locomotion policy using proximal policy optimization (PPO)[57], a model-free reinforcement learning algorithm widely used in legged locomotion tasks. Our environment is formulated as a partially observable Markov decision process (POMDP) since certain state information (e.g., contact forces and terrain) is unavailable. Consequently, the policy must infer missing states, increasing the complexity of learning. To address partial observability, previous studies have proposed stacking past observations or using architectures that capture historical information[8]. Similarly, we integrate recurrent neural network (RNN)-based architectures into the policy network to effectively capture and leverage temporal dependencies. We also employ an asymmetric actor-critic framework[55], allowing the critic—used only in simulation—to leverage privileged information. This setup ensures that the policy remains robust to partial observability while benefiting from the critic's guidance.

The locomotion of a legged robot involves numerous contact interactions, necessitating a simulator equipped with a fast and high-fidelity contact solver to enable effective transfer of policy from simulation to reality. To address this requirement, we used the Raisim simulator[50]. Detailed PPO hyperparameters and coefficients are listed in Extended Data Table. 2d.

Network architecture The network architecture for training the locomotion policy consists of an actor network that maps observations to actions and a critic network that estimates value functions. The actor network integrates a gated recurrent unit (GRU) with a multilayer perceptron (MLP). The GRU processes sensory observations as input, generating a hidden state that encapsulates enriched information. This hidden state, along with sensory observations and velocity commands, serves as input to the MLP, which maps these features to the actions. The critic network is implemented as an MLP that receives sensory observations, velocity commands, and privileged information as inputs and outputs the expected return. A detailed description of the network architecture is listed in Extended Data Table. 2a.

Observations and actions The actor network processes an observation consisting of the body roll-pitch vector, angular velocity, joint positions and velocities, and previous actions. These inputs are fed into the GRU layer, while the velocity command bypasses the GRU and is directly input to the MLP to prevent command history accumulation. The velocity command includes the desired linear velocities in the x- and y-directions and the angular velocity in the z-direction.

The critic network must include all observations related to the reward function to accurately predict the expected return and should incorporate as much information as possible to achieve full observability. Therefore, the observations of the critic network encompass all inputs used by the actor network, along with privileged information that is accessible only in simulation. This privileged information includes body linear velocity, foot contact state durations (swing time and stance time), body height, current and previous ground reaction forces, foot velocity prior to contact, contact states, foot contact normal angles, terrain type, and the local terrain height map. A detailed description of each input's dimensions is listed in Extended Data Table. 2b.

The action output is a 12-dimensional residual joint position offset, which is added to the nominal joint positions to generate the final joint position reference.

Rewards Legged robots, characterized by their high degrees of freedom and underactuated dynamics, require carefully designed reward functions to achieve natural motion. The primary objectives of our locomotion policy's reward function are accurate velocity command tracking, natural movement, and energy-efficient control. A complete list of reward terms is provided in the Extended Data Table. 3a. While many terms are derived from prior studies, this section focuses on three terms that significantly impact locomotion efficiency. For the ablation study, we conducted experiments with 4 m/s locomotion on a treadmill, as shown in Extended Data Fig. 4a and b. The loss analysis of this hardware experiment is presented in Extended Data Table. 3b.

Extended Data Fig. 4c-e illustrate the foot velocity profiles and pre-contact foot velocity histograms. These figures compare the proposed reward function with variants that exclude GRF smoothness and foot collision loss reward terms. Both terms contribute to minimizing mechanical losses by reducing the velocity at which the foot makes contact with the ground. This reduction directly mitigates foot collision losses, as demonstrated by the decrease in pre-contact foot velocities shown in the histograms.

Extended Data Fig. 4f-g present the torque profile of a single knee joint and torque histograms for all actuators, comparing the proposed method with a variant that omits magnetic saturation effects. By incorporating magnetic saturation, the current demand at torque levels exceeding the rated torque becomes proportional to the square of the torque. As a result, the proposed method limits torque utilization at higher levels, as indicated by the reduced histogram counts at elevated torque levels. This adjustment reduces actuator electric losses, enhancing overall energy efficiency.

Training Details At the beginning of each environment reset, we randomize the robot's body orientation, joint angles, generalized velocities, and velocity command. The initial linear and angular velocities of the robot's body are treated as external disturbances, allowing the agent to learn how to adapt and counteract the external wrench. The velocity command is uniformly

sampled within predefined ranges:

$$v_x,\ v_y,\ \omega_z \sim \mathcal{U}(-1, 4),\ \mathcal{U}(-1, 1),\ \mathcal{U}(-1, 1). \tag{10}$$

As training progresses through curriculum learning[47], the initial state distribution, velocity commands, and terrain difficulty incrementally increase in both complexity and range. The training environment incorporates three terrain types, classified based on the maximum contact normal angle between the foot and the ground, as shown in Extended Data Fig. 3b. The first terrain type includes *Hills* and *Slope*, characterized by maximum contact normal angles below 90 degrees, enabling the robot to learn locomotion on uneven surfaces. The second terrain type includes *Steps* and *Stairs*, characterized by a maximum contact normal angle of 90 degrees. In this scenario, the robot develops a foot-trapping reflex by lifting its foot higher when encountering an obstacle. The third terrain type includes *Stairs with nosing* and *Pipes*, where the maximum contact normal angle exceeds 90 degrees or involves shank contact. In this terrain, the robot learns to navigate steps by pulling its foot backward before swinging it forward. Detailed terrain parameters are provided in Extended Data Table. 2c.

To minimize the sim-to-real gap, we incorporated an action-regularizing loss[53]. Unlike prior approaches[54], we reduce reliance on extensive domain randomization, instead focusing on modeling sensor noise and joint friction.

Loss measurement

Total power measurement Total power consumption (P_{total}) is directly measured as battery voltage (V_{bat}) times battery output current (I_{bat}). We used this power measurement for TCOT calculations in two different contexts. For the marathon record, TCOT (0.248) was obtained by dividing the total energy consumption (1280 Wh) by the product of mass (45 kg, RAIBO with 2016 Wh), gravitational acceleration, and total distance (42.195 km). For detailed locomotion loss

analysis, we measured power during treadmill experiments where RAIBO2 maintained controlled constant speeds (Extended Data Fig. 4a and b). The average total power and TCOT were calculated from real-time logging data as:

$$P_{\text{total}} = \frac{\int_0^T V_{\text{bat}}(t) I_{\text{bat}}(t) dt}{T} \tag{11}$$

$$\text{TCOT} = \frac{P_{\text{total}}}{mgv_{\text{tredmill}}} \tag{12}$$

Battery voltage is measured using a voltage divider (383 kΩ/9.76 kΩ) and current via a hall effect sensor (Infineon ACS781LLRTR-100B-T), sampled at 15 kHz and transmitted at 2 kHz through EtherCAT[49]. This direct power measurement enabled validation of our detailed loss models by comparing P_{total} with the sum of individual loss components ($P_{\text{actuator,elect}}$, P_{mech}).

The motor copper loss ($P_{\text{m,copper}}$) calculation was based on the manufacturer's datasheet values, expressed as

$$P_{\text{m,copper}} = I_{\text{q}}^2 R_{\text{eff}} \tag{13}$$

where R_{eff} is derived from the TQ Motor ILM115x25 datasheet parameters (Extended Data Table. 1b). Using the specified torque constant ($k_{\text{T}} = 0.281$ Nm/A) and motor constant ($k_{\text{M}} = 0.87$ Nm/$\sqrt{\text{W}}$), the effective resistance was determined as $R_{\text{eff}} = k_{\text{T}}^2 / k_{\text{M}}^2 = 0.104\ \Omega$.

For driver loss characterization, we connected the motor stator without rotor to the driver and controlled the DC load current magnitudes to measure integrated power losses under various current levels. This setup eliminates motor iron losses by ensuring no time-varying magnetic fields: the absence of rotor prevents back-EMF generation, and steady-state DC current maintains constant magnetic fields. The total power consumption (P_{supply}) under these conditions consists of driver losses (P_{driver}) and motor copper losses ($P_{\text{m,copper}}$). By subtracting the known motor copper

losses from the total power measurement, we characterized the driver loss coefficients as:

$$P_{\text{supply}} - P_{\text{m,copper}} = P_{\text{driver}}(I) = a_0 + a_1 I + a_2 I^2 \tag{14}$$

where the fitted coefficients correspond to system loss ($a_0 = P_{\text{d,system}}$), switching loss ($a_1 I = P_{\text{d,switch}}$), and conduction loss ($a_2 I^2 = P_{\text{d,conduction}}$), respectively.

Motor iron losses result from magnetic field variations and consist of hysteresis and eddy current losses. Our model reflects only stator iron losses due to the relatively small magnitude of rotor iron losses in Permanent Magnet Synchronous Machines (PMSM)[58] and practical measurement limitations. To characterize the iron losses of the stator, we used only the stator assembly connected to the motor driver, applying virtual angle rotation to generate sinusoidal currents with varying frequencies and magnitudes. For sinusoidally varying magnetic flux density $B(I)$ with angular frequency ω_{s}, the iron loss density is expressed as:

$$P_{\text{supply}} - P_{\text{m,copper}} - P_{\text{driver}} = P_{\text{m,iron}}(I, \omega_s) = P_{\text{hys}} + P_{\text{eddy}} = k_{\text{h}} B^{\beta} \omega_{\text{s}} + k_{\text{e}} B^2 \omega_{\text{s}}^2 \tag{15}$$

where P_{hys} and P_{eddy} are hysteresis and eddy-current losses respectively, k_{h} and k_{e} are corresponding constants, and β is the Steinmetz constant[44,48].

Mechanical loss measurement Mechanical losses (P_{mech}) were calculated using real-time joint torque, speed, and position data recorded during treadmill experiments, combined with pre-characterized individual loss models. The mechanical loss consists of three components: joint friction loss (P_{joint}), slip loss (P_{slip}), and foot collision loss ($P_{\text{collision}}$). For constant velocity locomotion with zero body acceleration, we assumed that motors provide energy only to compensate for mechanical losses, as there is no net change in robot kinetic energy. The total mechanical loss can be calculated from motor output power, which is the product of torque and velocity. However, the torque calculation using $k_{\text{T}} i_{\text{q}}$ includes power that is lost to iron losses during magnetic

field conversion. Therefore, total mechanical loss was calculated by subtracting the previously determined iron losses from the motor output power as

$$P_{\text{mech}} = \sum_{i=1}^{12}(P_{\text{motor,output}}(i) - P_{\text{m,iron}}(i)) = \sum_{i=1}^{12}(k_{\text{T}} i_{\text{q}}(i)\omega_{\text{m}}(i) - P_{\text{m,iron}}(i)) \tag{16}$$

where k_{T} is the torque constant, $i_{\text{q}}(i)$ is the q-axis current, and $\omega_{\text{m}}(i)$ is the motor angular velocity of joint i.

The loss of joint friction results from the sliding contact between the gear teeth during power transmission. While friction is typically modeled as a function of load torque and speed, comprising both Coulomb and viscous friction components[40], we adopted only the Coulomb friction model due to experimental setup limitations. We characterize the friction torque as proportional to the applied torque through a friction coefficient, which was experimentally determined by measuring the torque difference between the input and output using an actuator-link assembly with end-point force measurement. The joint friction power loss was calculated as the product of friction torque and joint velocity:

$$P_{\text{joint}} = \sum_{i=1}^{12} \tau_{\text{friction}}(i) \cdot \omega(i) \tag{17}$$

where $\tau_{\text{friction}}(i)$ is the Coulomb model friction torque and $\omega(i)$ represents joint velocity.

The loss of foot collision occurs during the transitions of the foot from the swing to the stance phase. Assuming perfectly inelastic collisions with zero post-impact kinetic energy, the collision loss is calculated as

$$P_{\text{collision}} = \frac{1}{T_{\text{gait}}} \sum_{j=1}^{n} \frac{1}{2} v_{\text{j}}^{T} (JM^{-1}J^{T})^{-1} v_{\text{j}} \tag{18}$$

where T_{gait} represents the gait period, with v_{j} denoting the foot linear velocity vector before impact. J and M are the Jacobian matrix and robot mass matrix respectively, while n indicates the number of foot impacts per cycle.

Slip loss, occurring from foot slippage during stance phase, presents calculation challenges due to the difficulty in precisely measuring instantaneous normal forces and friction coefficients. Therefore, we quantified it as the residual mechanical loss after subtracting other known components. Slip loss term used in this paper includes both actual slippage losses and other unmodeled mechanical losses in the system, represented as

$$P_{\text{slip}} = P_{\text{mech}} - P_{\text{collision}} - P_{\text{joint}} \tag{19}$$

Method references

[47] Yoshua Bengio, Jérôme Louradour, Ronan Collobert, and Jason Weston. Curriculum learning. In Proceedings of the 26th annual international conference on machine learning, pages 41–48, 2009.

[48] G. Bertotti. General properties of power losses in soft ferromagnetic materials. IEEE Transactions on Magnetics, 24(1):621–630, 1988.

[49] EtherCAT Technology Group. Ethercat - the ethernet fieldbus. Online: `https://www.ethercat.org/default.htm`, 2024. The open real-time Ethernet network technology organization.

[50] Jemin Hwangbo, Joonho Lee, and Marco Hutter. Per-contact iteration method for solving contact dynamics. IEEE Robotics and Automation Letters, 3(2):895–902, 2018.

[51] Infineon Technologies AG. Eicedriver™ high voltage gate driver ic evaluation board. Application Note EVAL_6EDL04N02PR, Infineon Technologies AG, 81726 Munich, Germany, July 2013. Document Revision 1.0.

[52] Chunting Mi, G.R. Slemon, and R. Bonert. Modeling of iron losses of permanent-magnet synchronous motors. IEEE Transactions on Industry Applications, 39(3):734–742, 2003.

[53] Siddharth Mysore, Bassel Mabsout, Renato Mancuso, and Kate Saenko. Regularizing action policies for smooth control with reinforcement learning. In 2021 IEEE International Conference on Robotics and Automation (ICRA), pages 1810–1816. IEEE, 2021.

[54] Xue Bin Peng, Marcin Andrychowicz, Wojciech Zaremba, and Pieter Abbeel. Sim-to-real transfer of robotic control with dynamics randomization. In 2018 IEEE International Conference on Robotics and Automation (ICRA), pages 3803–3810, 2018.

[55] Lerrel Pinto, Marcin Andrychowicz, Peter Welinder, Wojciech Zaremba, and Pieter Abbeel. Asymmetric actor critic for image-based robot learning. arXiv preprint arXiv:1710.06542, 2017.

[56] Marc H. Raibert and Ernest R. Tello. Legged robots that balance. IEEE Expert, 1(4):89–89, 1986.

[57] John Schulman, Filip Wolski, Prafulla Dhariwal, Alec Radford, and Oleg Klimov. Proximal policy optimization algorithms. arXiv preprint arXiv:1707.06347, 2017.

[58] Wenming Tong, Shengnan Wu, Jingyang Sun, and Longfei Zhu. Iron loss analysis of permanent magnet synchronous motor with an amorphous stator core. In 2016 IEEE Vehicle Power and Propulsion Conference (VPPC), pages 1–6, 2016.

Data availability All data presented in the paper are available at https://doi.org/10.5281/zenodo.14825866.

Code availability Simulation code for RAIBO2 locomotion is available upon reasonable request.

Acknowledgments Funding: This work was supported by the Samsung Research Funding and Incubation Center of Samsung Electronics under Project Number SRFC-IT2002-02.

Competing Interests The authors declare that they have no competing financial interests.

Author Contributions C.L., D.Y., J.P. and J.H. designed the research and analyzed the data. C.L. designed the electrical system, D.Y. trained the control policy, and J.P. designed the mechanical hardware. C.L., J.L., S.C., G.J., J.M., and J.H. developed the robot software. C.L., D.Y., J.P., J.L., S.C., G.J., J.M., M.J., H.C., H.K., H.O., K.N., M.L., J.H., D.C., D.K., and Y.A. assisted in designing the experimental setup and supporting the marathon performance evaluation. C.L., D.Y., J.P., J.L., and J.H. co-wrote the manuscript. All authors gave final approval for publication.

Correspondence Correspondence and requests for materials should be addressed to jhwangbo@kaist.ac.kr.

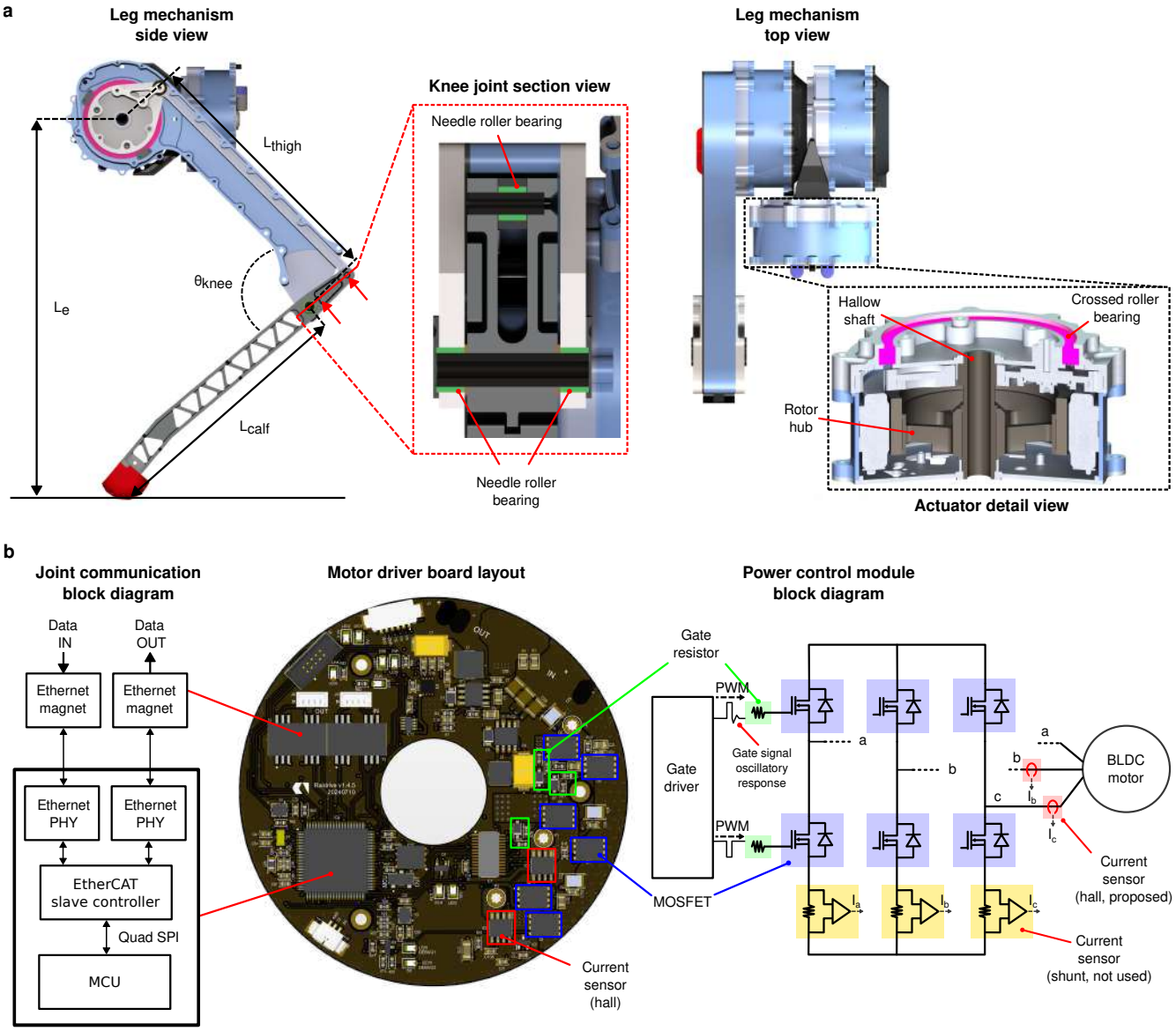

Extended Data Fig. 1 | Design implementations for leg mechanism and motor driver circuit. **a,** Lightweight leg mechanism design featuring knee joint and actuator design. **b,** Motor driver system showing integrated communication processor layout and power control module with MOSFET arrangement and current sensor implementations.

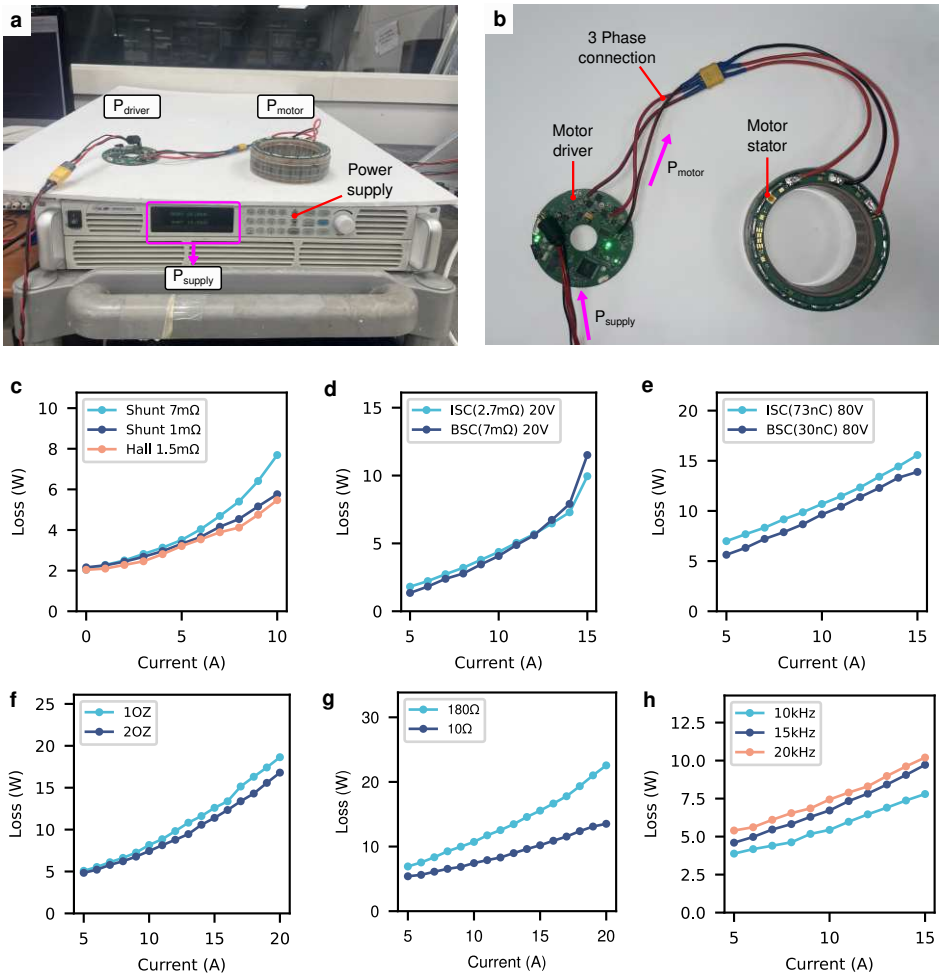

Extended Data Fig. 2 | Systematic approach to motor driver loss reduction through sequential design improvements. a,b, Experimental setup for loss measurements: complete test bench configuration (a) and integrated motor driver-stator system (b). **c-h,** Comprehensive loss characterization across design parameters: current sensing method comparison (c), MOSFET conduction loss analysis at low voltage operation (20V) (d), MOSFET switching loss analysis at high voltage operation (80V) (e), PCB copper thickness effects (f), gate resistance modification (g), and switching frequency impact (h).

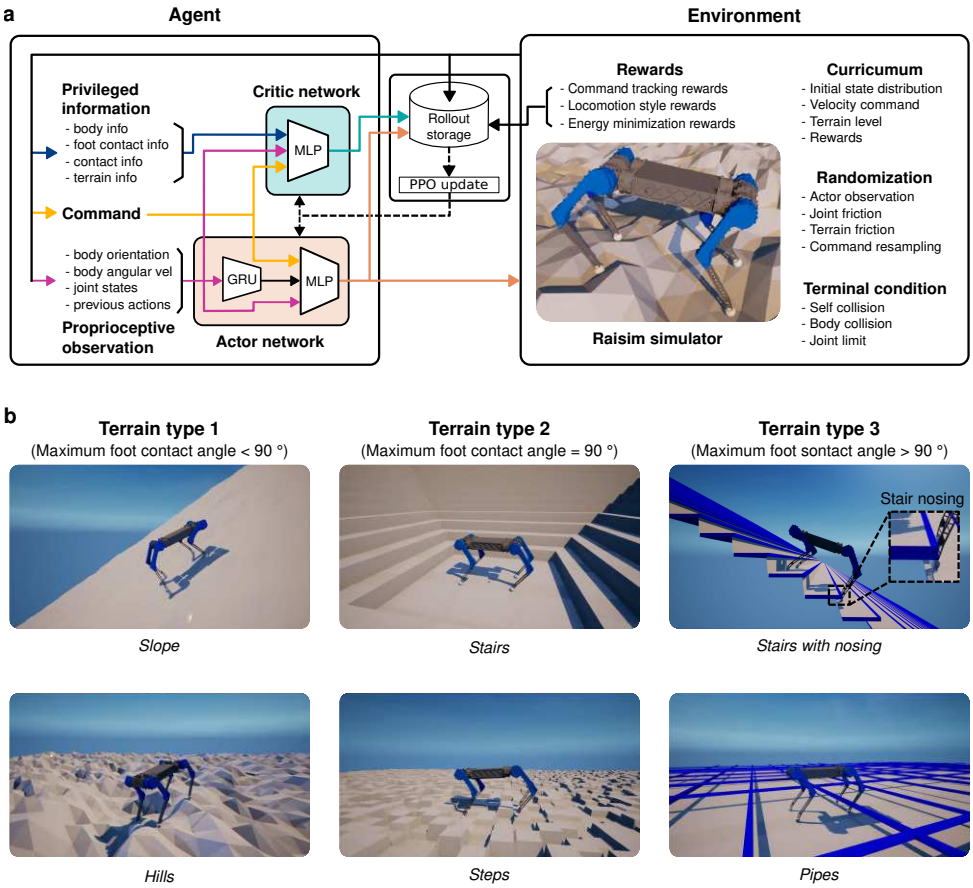

Extended Data Fig. 3 | Reinforcement learning framework and terrain classification for locomotion policy development. a, Detailed system architecture showing agent networks (privileged information, proprioceptive observation, actor-critic networks) and environment elements (simulator, rewards, curriculum). **b,** Training environments classified into three terrain types based on maximum foot contact angle: *slopes* and *hills* (Type 1), standard *stairs* and *steps* (Type 2), and *stairs with nosing* and *pipes* (Type 3).

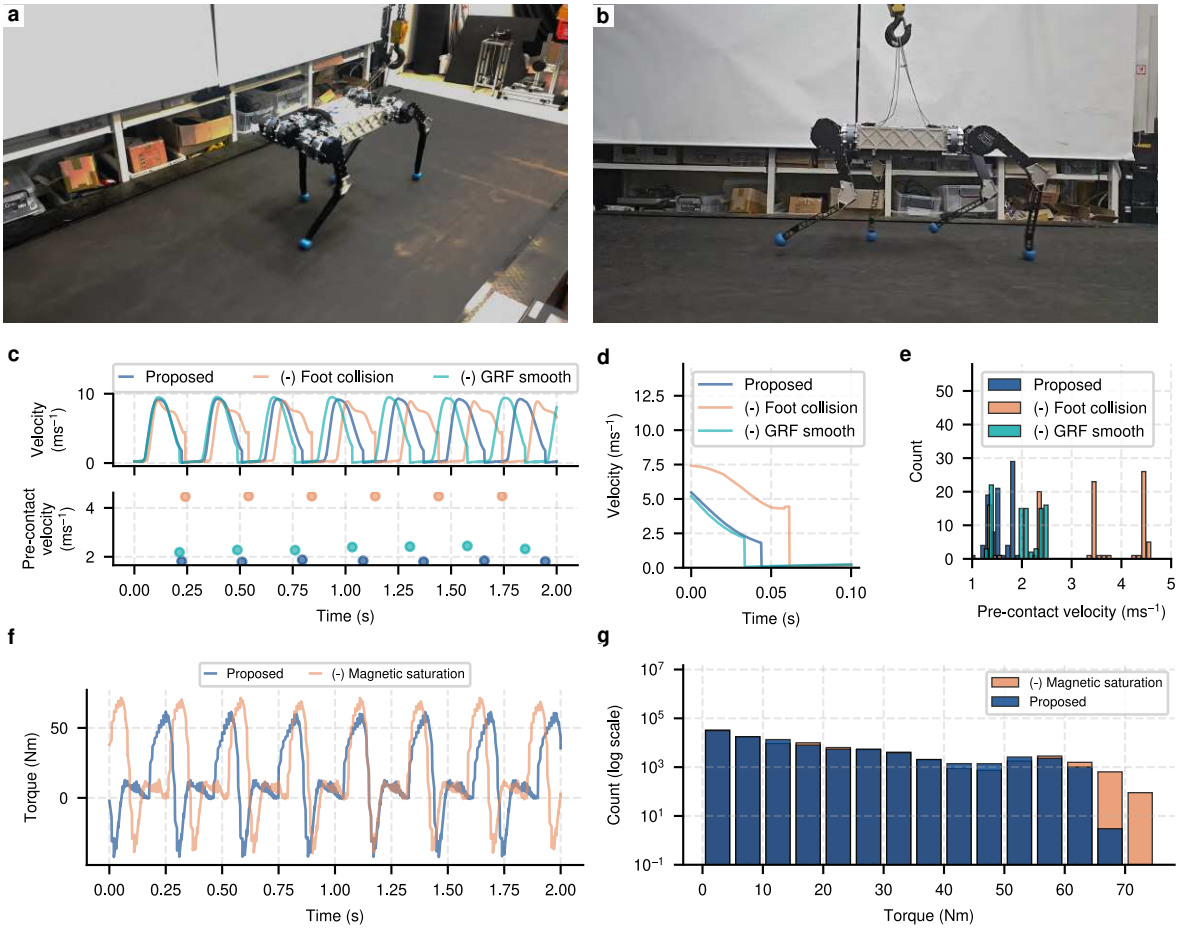

Extended Data Fig. 4 | Experimental validation of locomotion policy for efficiency improvement. a,b, RAIBO2 running at controlled speed on treadmill for efficiency measurements (Supplementary Video 2 and 3). **c,d,** Comparison of foot velocity profiles between proposed and baseline controllers, with detailed view of contact moment (d). **e,** Pre-contact velocity distribution histogram across different control strategies. **f,** Knee joint torque profiles demonstrating the effect of magnetic saturation reward. **g,** Torque distribution histogram comparing policies with and without magnetic saturation reward consideration.

a

RAIBO2 Specification	Value	Percentage
Weight		
Total weight (1512 Wh / 2016 Wh)	43.0 kg / 45.0 kg	100%
Actuation parts (12 × 2.0 kg)	24.0 kg	55.8%
Battery (1512 Wh / 2016 Wh)	6.5 kg / 8.6 kg	15.1%/19.1%
Legs (4 × 1.1 kg)	4.4 kg	10.2%
Etc	8.1 kg	18.9%
Dimension		
Length	970 mm	–
Width	425 mm	–
Height (with full leg stretch / nominal)	630 mm / 550 mm	–
Leg thigh length (L_{thigh})	320 mm	–
Leg calf length (L_{calf})	320 mm	–

b

Motor Specification (Interconnection Star-Serial)		
Parameter	**Value**	**Unit**
General Data / Basic Data		
Power P	570	W
Rated torque T_r	3.9	Nm
Peak torque T_{max} @ 20% linearity deviation	12.7	Nm
Speed n_{max}	1400	rpm
Weight m	1070	g
Performance Characteristics		
Rated voltage U_r	48	V
Rated current I_r (phase current amplitude)	14.1	A
Copper losses P_{copper} @ T_r and 20℃	20.9	W
Torque constant k_T @ 20℃	281	mNm/A
Terminal resistance R_{TT} @ 20℃	140	mΩ
Terminal inductance L_{TT}	600	μH
Motor constant k_M @ 20℃	0.87	Nm/$\sqrt{\text{W}}$
Rotor inertia J	3.93	kgcm^2
Number of pole pairs	15	–
Max. Efficiency η	93	%
Dimensions		
Outer diameter of stator	115	mm
Length Stator	39.0	mm
Inner diameter rotor	74	mm
Length Rotor	27.1	mm

Extended Data Table. 1 | RAIBO2 robot and motor specifications. a, RAIBO2 weight distribution and dimensions. **b,** TQ group ILM115x25 Motor specification.

a

Module	Type	Inputs	Hidden Layers	Outputs
Actor network	GRU	$\mathbf{o}_t$	[128]	$\mathbf{h}^t$
	MLP	$\mathbf{o}_t, \mathbf{h}_t, \mathbf{v}_t^{\text{cmd}}$	[256, 128]	$\mathbf{a}_t$
Critic network	MLP	$\mathbf{o}_t, \mathbf{p}_t, \mathbf{h}_t, \mathbf{v}_t^{\text{cmd}}$	[512, 256, 128]	V_t

b

Type	Dim	Observations	Noise (σ)
$\mathbf{o}_t$	3	Body orientation	0.033
	3	Body angular velocity	0.22
	12	Joint position	0.055
	12	Joint velocity	0.55
	12	Previous action	
$\mathbf{v}_t^{\text{cmd}}$	3	Velocity command	
$\mathbf{p}_t$	3	Body linear velocity	
	4	Swing time	
	4	Stance time	
	1	Body height	
	4	Ground reaction force	
	4	Previous ground reaction force	
	4	Foot velocity prior to contact	
	16	Contact states	
	4	foot contact normal angle	
	3	terrain type	
	36	Terrain heights	

c

Terrain Type	Terrain	Params	Range
0	*Hills*	Frequency	[0.2, 1.0]
		Amplitude (m)	[0.2, 1.4]
	Slope	Frequency	[0.2, 0.8]
		Amplitude (m)	[0.2, 0.6]
		Angle (°)	[0, 35]
1	*Steps*	Width (m)	[0.1, 0.5]
		Height (m)	[0.02, 0.18]
	Stairs	Width (m)	[0.28, 0.32]
		Height (m)	[0.02, 0.18]
2	*Stairs with nosing*	Width (m)	[0.28, 0.32]
		Height (m)	[0.02, 0.18]
		Nosing projection (m)	[0.02, 0.04]
	Pipes	Height (m)	[0.045, 0.21]
		Width (m)	[0.03, 0.06]
		interval (m)	[0.9, 1.1]

d

Parameter	Value
simulation frequency (Hz)	400
control frequency (Hz)	100
max. episode length	400
discount factor	0.99
GAE-λ	0.95
epochs	32
batch size	80000
total iteration	50000
initial learning rate	5e-4
learning rate decay	StepLR(0.9999)
clip ratio	0.2

Extended Data Table. 2 | Network parameters and training hyperparameters. a, Network architectures. **b,** Dimension of proprioceptive observation and privileged information. **c,** Terrain parameters. **d,** Hyperparameters for policy training.

a

Category	Reward	Equation	Scale
Command Reward	Command Tracking	$e^{-\|\mathbf{v}_{xy}^{\text{cmd}}-\mathbf{v}_{xy}\|^2} \cdot (1+e^{-0.5\|\mathbf{v}_{xy}^{\text{cmd}}-\mathbf{v}_{xy}\|}) + e^{-1.5(\omega_z^{\text{cmd}}-\omega_z)^2}$	1.5
Locomotion Style Reward	Body Height	$e^{-10\lvert h_{\text{target}}-h_{\text{body}}\rvert}$	0.5
	Swing / Stance Time	$\min(t_{\text{swing}}, 0.2) + \min(t_{\text{stance}}, 0.2)$	0.9
	Nominal Foot Position	$\|\mathbf{p}_{\text{foot}_{xy}} - \mathbf{p}_{\text{foot}_{xy}}^{\text{nominal}}\|$	-2.0
	Roll Joint Position	$\sum_{i=1}^{n_{\text{legs}}} q_{3i}^2 \lvert v_x\rvert / \|\mathbf{v}^{\text{cmd}}\|$	-2.5
	Swing Foot Clearance	$(p_{\text{foot}_z} - p_{\text{foot}_z}^{\text{target}})^2 \|\mathbf{v}_{\text{foot}}\| \mathbf{1}_{\text{swing}} / (0.2 + \|\mathbf{v}^{\text{cmd}}\|)$	-120.0
	Flight Phase	$\prod_{i=1}^{n_{\text{legs}}} \mathbf{1}_{i_{\text{swing}}}$	-2.0
	Joint Limit	log barrier$(\mathbf{q}, \mathbf{q}_{\text{upper}}, \mathbf{q}_{\text{lower}})$	-1.0
Energy Minimization Reward	Actuator Joule Loss	$\sum_{i=1}^{n_{\text{joints}}} (a_1 \lvert I_i\rvert + a_2 I_i^2) \;\; (I \propto \tau^2)$	-2.0e-3
	Foot Collision Loss	$\|\mathbf{v}_{\text{foot}}(\text{before contact})\| \mathbf{1}_{\text{contact}}$	-0.4
	Slip Loss	$\|\mathbf{v}_{\text{foot}_{xy}}\|^2 \mathbf{1}_{\text{contact}}$	-8.0e-2
	Body Stabilize	$v_z^2 + 0.02\lvert\omega_x\rvert + 0.02\lvert\omega_y\rvert$	-20.0
	Joint Velocity	$\|\dot{\mathbf{q}}\|^2$	-1.6e-3
	Joint Acceleration	$\|\ddot{\mathbf{q}}\|^2$	-1.0e-2
	Action Smoothness	$\|\mathbf{a}_{t-2} + \mathbf{a}_t - 2\mathbf{a}_{t-1}\|^2 + 0.5\|\mathbf{a}_t - \mathbf{a}_{t-1}\|^2$	-10.0
	GRF Smoothness	$0.5\|\mathbf{GRF}_{t-2} + \mathbf{GRF}_t - 2\mathbf{GRF}_{t-1}\|^2 + \|\mathbf{GRF}_t - \mathbf{GRF}_{t-1}\|^2$	-3.0e-6

b

Policy	Actuator Electric Loss	Mechanical Loss	System Loss	Total Loss
Proposed	284.6	120.9	41.7	447.2
Proposed ⊖ GRF Smoothness	279.8	151.3	40.0	471.0
Proposed ⊖ Magnetic Saturation	299.4	149.2	44.9	493.4
Proposed ⊖ Foot Collision Loss	324.6	272.1	26.4	623.1

Extended Data Table. 3 | Reward functions and ablation study. a, Reward functions. **b,** Loss distribution by reward ablation at 4 m/s locomotion.

a

No.	MOSFET	Voltage	Switching Frequency	Gate Resistor	PCB Copper	Current Sensing Method
c	BSC	20 V	20 kHz	180 Ω	1 oz	**7mΩ(S), 1mΩ(S), 1.5mΩ(H)**
d	**BSC, ISC**	20 V	20 kHz	180 Ω	1 oz	1.5mΩ(H)
e	**BSC, ISC**	80 V	20 kHz	180 Ω	2 oz	1.5mΩ(H)
f	BSC	80 V	20 kHz	10 Ω	**1 oz, 2 oz**	1.5mΩ(H)
g	ISC	80V	20 kHz	**10 Ω, 180 Ω**	2 oz	1.5mΩ(H)
h	ISC	80 V	**10 kHz, 15 kHz, 20 kHz**	10 Ω	2 oz	1.5mΩ(H)

b

	BSC070N10NS5SC	ISC022N10NM6	Unit
Package	SuperSO8 5x6	SuperSO8 5x6	
$V_{DS,max}$	100	100	V
$R_{DS,on}$	7.0	2.24	m Ω
$I_{D,max}$	82	230	A
Q_{OSS}	41	135	nC
Q_G	30	73	nC

Extended Data Table. 4 | Driver ablation study experimental conditions and MOSFET specifications. a, Driver ablation study experimental conditions. **b,** MOSFET specifications.

Supplementary Files

This is a list of supplementary files associated with this preprint. Click to download.

- SupplementaryInformation.zip